



Measuring the Progenitor Masses and Dense Circumstellar Material of Type II Supernovae

Viktoriya Morozova¹, Anthony L. Piro² , and Stefano Valenti³

¹ Department of Astrophysical Sciences, Princeton University, Princeton, NJ 08544, USA; vsg@astro.princeton.edu

² The Observatories of the Carnegie Institution for Science, 813 Santa Barbara St., Pasadena, CA 91101, USA

³ Department of Physics, University of California, Davis, CA 95616, USA

Received 2017 September 14; revised 2018 February 22; accepted 2018 March 23; published 2018 April 27

Abstract

Recent modeling of hydrogen-rich Type II supernova (SN II) light curves suggests the presence of dense circumstellar material (CSM) surrounding the exploding progenitor stars. This has important implications for the activity and structure of massive stars near the end of their lives. Since previous work focused on just a few events, here we expand to a larger sample of 20 well-observed SNe II. For each event we are able to constrain the progenitor zero-age main-sequence (ZAMS) mass, explosion energy, and the mass and radial extent of the dense CSM. We then study the distribution of each of these properties across the full sample of SNe. The inferred ZAMS masses are found to be largely consistent with a Salpeter distribution with minimum and maximum masses of 10.4 and $22.9 M_{\odot}$, respectively. We also compare the individual ZAMS masses we measure with specific SNe II that have pre-explosion imaging to check their consistency. Our masses are generally comparable to or higher than the pre-explosion imaging masses, potentially helping ease the red supergiant problem. The explosion energies vary from $(0.1\text{--}1.3) \times 10^{51}$ erg, and for $\sim 70\%$ of the SNe we obtain CSM masses in the range between 0.18 and $0.83 M_{\odot}$. We see a potential correlation between the CSM mass and explosion energy, which suggests that pre-explosion activity has a strong impact on the structure of the star. This may be important to take into account in future studies of the ability of the neutrino mechanism to explode stars. We also see a possible correlation between the CSM radial extent and ZAMS mass, which could be related to the time with respect to explosion when the CSM is first generated.

Key words: hydrodynamics – radiative transfer – supernovae: general

1. Introduction

A longstanding problem in the study of explosive transient events is connecting classes of supernovae (SNe) to the specific progenitors that generate them. In this sense, hydrogen-rich Type II SNe might be thought to be the most straightforward link for making this connection. With the exception of the rarer Type I Ib and 1987A-like events, pre-explosion imaging obtained with the *Hubble Space Telescope* exclusively identifies red supergiants (RSGs) as their progenitors (Li et al. 2006; Smartt et al. 2009; Van Dyk et al. 2012). These are expected to largely evolve as single stars, so that their models can be generated without many of the complications present for other stellar calculations (such as binarity or a high spin). This in turn should simplify explosion and light-curve calculations, which find that an RSG naturally produces the plateau-shaped light curve of SNe II with the recombination of many solar masses of hydrogen-rich material with an RSG-like radius (Smith et al. 2011; Dessart et al. 2013; Utrobin & Chugai 2013; González-Gaitán et al. 2015; Rubin & Gal-Yam 2017; Renzo et al. 2017).

Nevertheless, many outstanding questions remain about how Type II progenitors connect to their light curves. Chief among these is the relationship between the Type IIP (plateau) and Type IIL (linear) subclasses, which is based on the shape of their light curves during the first few weeks (Barbon et al. 1979). There has been a long debate on whether there is a physical variable that smoothly transitions between Type IIP and IIL, or if a specific mechanism creates this dichotomy more abruptly. There have been some claims of distinct populations (Arcavi et al. 2012; Faran et al. 2014a, 2014b), but support for the more continuous case has increased as larger compilations by Anderson et al. (2014) and Sanders et al. (2015) showed a more continuous

range of early light-curve slopes. An important breakthrough came when Valenti et al. (2015) demonstrated that if one simply follows an SN IIL long enough, its light curve will drop at ~ 100 days, just like a normal SN IIP (previous SNe IIL studies rarely followed the light curve beyond ~ 80 days from discovery; see also Anderson et al. 2014). This suggests that Type IIL and Type IIP SNe may have a similar amount of hydrogen present for the main bulk of their envelopes, and whatever is creating the Type IIL distinction may be contributing something above a fairly normal underlying RSG.

Motivated by these issues, Morozova et al. (2017) recently numerically modeled three Type II SNe with extensive photometry over many wavebands by using RSG models with dense CSM stitched on top of them. This work was different from previous theoretical studies (e.g., Moriya et al. 2011) in that the CSM was generally more massive and compact (only extending a few stellar radii above the RSG). The two important conclusions from this work were that (i) this dense CSM could naturally explain the photometric differences between the Type IIP and IIL, and (ii) even the seemingly more normal Type IIP SNe need dense CSM to accurately model their light curves. It is still unclear what the full implications of these results are. It seems to indicate that there is increased activity in RSGs during the last months or years of their lives, which may be related to theoretical studies of pre-explosion outbursts (Quataert & Shiode 2012; Shiode & Quataert 2014; Quataert et al. 2016; Fuller 2017). Furthermore, observations of SNe II shortly after explosion show narrow lines that indicate a dense wind-like environment (e.g., Yaron et al. 2017), albeit probing more extended and less dense material than the CSM we need for the light curves (Dessart et al. 2017). This in turn brings up the question of whether there is a relationship between these two components of the CSM (Moriya et al. 2017).

An important step toward better understanding this dense CSM is mapping out its diversity over a larger sample of SNe II. With this goal in mind, we extend our previous work on SN II light-curve modeling to a set of 20 especially well-observed events. This allows us to measure the mass and extent of the dense CSM, constrain the zero-age main-sequence (ZAMS) masses, and measure the explosion energies. From this we can derive better constraints on just how common this dense CSM is (at least 70% of our sample), as well as look for correlations between the various properties that may provide clues to the dense CSM origin. Beyond just the CSM properties, because we are able to constrain the ZAMS masses for a wide sample, this provides important complementary information about SN II progenitors to other studies of RSGs (e.g., work on pre-explosion imaging, Smartt 2009; Smartt et al. 2009).

In Section 2 we describe the details of our simulations. The sample of 20 SNe II used for this work is presented in Section 3 along with our modeling strategy and fitting results. In Section 4 we explore what we can learn with our full sample of fits and search for correlations between different properties of the SN progenitors that we measure. In Section 5 we summarize our results and discuss future work.

2. Numerical Setup

As in our previous work (Morozova et al. 2017), we use the non-rotating solar-metallicity RSG models from the stellar evolution code KEPLER (Weaver et al. 1978; Woosley & Heger 2007, 2015; Sukhbold & Woosley 2014; Sukhbold et al. 2016). Above these models we add a CSM extending out to a radius R_{ext} with the density profile of a steady-state wind,

$$\rho(r) = \frac{\dot{M}}{4\pi r^2 v_{\text{wind}}} = \frac{K}{r^2}, \quad (1)$$

where \dot{M} is the wind mass-loss rate and v_{wind} is the wind velocity. A steady-state wind is widely used in the literature to describe the structure of CSM in the vicinity of RSGs (Chugai et al. 2007; Ofek et al. 2010; Chevalier & Irwin 2011; Moriya et al. 2011), and we use it as a convenient prescription to explore the diversity of possible CSM properties with just two parameters, K and R_{ext} (the case of an accelerating wind is considered in Moriya et al. 2017, while for the cases of exponential or power-law density distributions, see Nagy & Vinkó 2016). We assume the temperature and composition of the CSM to be constant and equal to their values at the surface of the underlying RSG models. In this work, we do not address the physical mechanism responsible for the formation of the CSM, which is crucial in defining the details of its structure. Instead, we concentrate on the general characteristics of the CSM, such as its total mass M_{CSM} and extent R_{ext} . Numerical studies of extended material around SNe demonstrate that the exact density distribution is only of secondary importance to these main properties (e.g., Piro et al. 2017).

From the large set of progenitor models presented in Sukhbold et al. (2016), we choose a subset of models in the mass range between 9 and $25 M_{\odot}$ in steps of $0.5 M_{\odot}$. Despite uncertainties in the upper limit (Smartt et al. 2009; Smith et al. 2011; Groh et al. 2013; Dwarkadas 2014), the stars in this range of ZAMS masses are believed to be progenitors of the bulk of Type II SNe. To obtain light curves from these models, we explode them with our open-source numerical code SNEC (Morozova et al. 2015) in

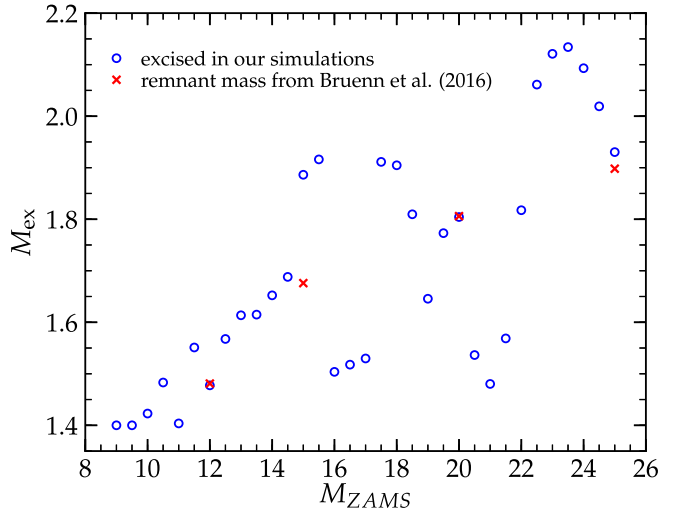


Figure 1. Excised mass as a function of ZAMS mass in our simulations (blue circles), which is taken to be equal to the mass coordinate of the silicon–oxygen interface in the pre-collapse composition profile. For comparison, in red we show the baryonic rest masses of proto-neutron stars formed in core-collapse SN explosion mechanism simulations by Bruenn et al. (2016) using progenitor models of Woosley & Heger (2007).

the range of asymptotic explosion energies, E_{fin} , between 0.04 and 1.3 B in steps of 0.02 B, where 1 B = 10^{51} erg. We use a thermal bomb mechanism for the explosions, where the thermal bomb energy, E_{bomb} , is found from E_{fin} and the total pre-explosion (negative, mostly gravitational) energy of the model, E_{init} , as $E_{\text{bomb}} = E_{\text{fin}} - E_{\text{init}}$. This energy is then injected into the inner $0.02 M_{\odot}$ of the model for a duration of 1 s. Previous work discusses the impact of this duration choice (Morozova et al. 2015, 2016, 2017). Exploding higher mass progenitors with low energies is challenging for our code, since the current version is not capable of treating material falling back onto a remnant. Therefore, a region of the parameter space is not covered in our study (shown in Figure 4 as a gray shaded area).

Before exploding the models, we excise the inner part, which is assumed to form a neutron star. As shown in the large number of SN explosion mechanism simulations (e.g., Müller et al. 2012; Burrows et al. 2018; Summa et al. 2016; Suwa et al. 2016; Radice et al. 2017), the passage of the otherwise stalled shock wave through the density and composition discontinuities of the progenitor model, such as the boundary between the silicon- and oxygen-burning shells, can facilitate its revival and play an important role in the successful SN explosion. Therefore, one can expect the remnant masses to be equal to or slightly higher than the mass coordinate of the Si/O interface in the progenitor composition profile, and we use this as a criterion to determine the excised mass in our simulations. Figure 1 shows the excised mass as a function of ZAMS mass for our subset of models. The values of the baryonic rest mass of the proto-neutron stars from the simulations of Bruenn et al. (2016), using progenitor models from Woosley & Heger (2007), are shown for comparison. Higher excision masses facilitate the explosion of high ZAMS mass progenitors to some extent. We note, however, that as long as the explosion is successful, the light curve depends very weakly on the excised mass.

In SNEC, we use the equation of state by Paczyński (1983) and solve for the ionization fractions of hydrogen and helium

Table 1
Observed SN Parameters

SN	DM	ΔDM	$A_{B,i}$ [mag]	$A_{B,g}$ (mag)	t_{PT} (d)	Δt_{PT} (d)	t_s (d)	M_{Ni} [M_\odot]	ΔM_{Ni} [M_\odot]
1999em	30.34	0.07	0.234	0.174	118.1	1.0	34.4	0.0536	0.0119
1999gi	30.34	0.14	0.0	0.07	127.8	3.1	38.2	0.0320	0.0023
2001X	31.59	0.11	0.0	0.173	114.7	5.0	41.9	0.0550	0.0047
2003Z	31.70	0.15	0.0	0.141	124.2	4.5	29.4	0.0047	0.0002
2003hn	31.14	0.26	0.71	0.057	106.9	4.0	42.8	0.0324	0.0046
2004et	28.36	0.09	0.03	1.48	123.5	4.0	53.4	0.0414	0.0086
2005cs	29.26	0.33	0.0	0.205	126.0	0.5	22.3	0.0021	0.0002
2009N	31.67	0.11	0.532	0.078	108.3	1.2	26.6	0.0165	0.0021
2009ib	31.48	0.31	0.537	0.105	140.1	2.0	38.1	0.0520	0.0162
2012A	29.96	0.15	0.05	0.1	106.5	2.0	28.4	0.0087	0.0012
2012aw	29.96	0.09	0.24	0.115	135.2	4.0	36.6	0.0497	0.0059
2012ec	31.32	0.15	0.414	0.096	107.9	5.0	36.3	0.0394	0.0051
2013ab	31.90	0.08	0.081	0.099	101.8	1.0	36.4	0.0588	0.0100
2013by	30.81	0.15	0.0	0.798	85.4	2.0	39.7	0.0320	0.0043
2013ej	29.79	0.20	0.0	0.25	98.8	1.0	38.4	0.0207	0.0019
LSQ13dpa	35.08	0.15	0.0	0.137	128.7	2.0	36.9	0.0714	0.0127
2014cy	31.87	0.15	0.0	0.2	122.6	1.0	33.0	0.0037	0.0038
ASASSN-14dq	33.26	0.15	0.0	0.254	101.0	5.5	33.6	0.0461	0.0079
ASASSN-14gm	31.74	0.15	0.0	0.406	110.6	1.5	43.3	0.0767	0.0102
ASASSN-14 ha	29.53	0.50	0.0	0.033	136.8	1.5	37.5	0.0014	0.0002

following the approach of Zaghoul et al. (2000). The numerical grid is identical to the one used in our previous studies and consists of 1000 cells (Morozova et al. 2015, 2016, 2017). We use the same prescription for the opacity floor as in those works, namely, $0.01 \text{ cm}^2 \text{ g}^{-1}$ for the solar metallicity $Z = 0.02$, and $0.24 \text{ cm}^2 \text{ g}^{-1}$ for $Z = 1$, with the linear dependence in between. We smoothen the composition profiles before the explosion by passing a boxcar with a width of $0.4 M_\odot$ through the models four times. Photometric light curves are calculated assuming blackbody emission and using the MATLAB package for astronomy and astrophysics for calculating specific wavebands (Ofek 2014).

3. Numerical Models of 20 SNe II

3.1. Observational Data

The SN sample we analyze here was chosen from a collection of high-quality SN II light curves presented in Valenti et al. (2016). The two main criteria we used in selecting them were (i) a good multiband light-curve coverage, and (ii) an estimate of the ^{56}Ni mass from the radioactive tail. We have omitted a few SNe due to the large uncertainty in the explosion date (>6 days) as well as the lack of data points during the transition between the plateau and the radioactive tail, both of which are important to obtain good quality fits using our approach.

Table 1 summarizes the observed properties of the selected SN sample. The distance modulus, DM, together with its uncertainty, ΔDM , are taken from Table 2 of Valenti et al. (2016). The interstellar and galactic values of the absorption in B band, $A_{B,i}$ and $A_{B,g}$, respectively, are used to correct the light curves for reddening according to the Cardelli law (Cardelli et al. 1989).⁴ The plateau length t_{PT} is obtained by fitting a

⁴ Note that the interstellar reddening shown in Table 1 was estimated based on the equivalent width of Na I D lines in the spectra of host galaxies and does not take into account possible extinction due to circumstellar dust. However, since circumstellar dust is likely destroyed by the SN explosion, it should not affect the light-curve modeling. Negligible interstellar reddening for some SNe from the sample is additionally supported by the fact that they have similar colors during the plateau phase.

Fermi–Dirac function to the transition between the plateau and radioactive tail, and Δt_{PT} is its uncertainty.⁵ The ^{56}Ni mass, M_{Ni} , and its uncertainty, ΔM_{Ni} , were derived in Valenti et al. (2016) from the comparison of the post-plateau pseudo-bolometric light curves to the one of SN 1987A.

It has been highlighted in some observational work that some SN light curves demonstrate a change in slope at a few tens of days after the maximum (Anderson et al. 2014; Valenti et al. 2016). This change is more pronounced in the pseudo-bolometric light curves (including bands from U/B to I) than in the single bands. The time t_s in Table 1 marks the last data point used to measure the early slope of the pseudo-bolometric light curves of the corresponding SNe in Valenti et al. (2016; the first parameter ph_stop in their Table D4), which we use here as a proxy for the transition time between the early faster and the late shallow slopes.

3.2. Two-step Approach to Numerical Modeling

As discussed in Section 1, recent work demonstrates that a dense, compact CSM is crucial for modeling Type II SN light curves (Morozova et al. 2017). This means that properly fitting these light curves requires fitting for M_{ZAMS} , E_{fin} , M_{Ni} , ^{56}Ni mixing, explosion time, R_{ext} , and K —a seven-parameter fitting space! Since building such a larger grid of models is simply not feasible, we take advantage of the knowledge that the early light curve over the first ~ 10 –30 days should be dominated by the CSM, and that the remainder of the light curve is dominated by the hydrogen-rich RSG envelope. This allows us to use a two-step approach in fitting the SN light curves, which we describe further below.

In the first step of our light-curve fitting, we generate a grid of light curves in $M_{\text{ZAMS}}\text{--}E_{\text{fin}}$ parameter space, in each case using the radioactive ^{56}Ni mass for each SN from Table 1. As was discussed in Section 2, we cover the parameter space $9 M_\odot < M_{\text{ZAMS}} < 25 M_\odot$ in steps of $0.5 M_\odot$ and $0.04 \text{ B} < E_{\text{fin}} < 1.3 \text{ B}$ in steps of 0.02 B (with the exception

⁵ The values of t_{PT} are taken from Table D5 of Valenti et al. (2016) when available, otherwise from Table D4.

of the highest masses and lowest energies). To account for the effect of ^{56}Ni mixing into the envelope, we consider three degrees of ^{56}Ni mixing for each SN, up to the mass coordinates of 3, 5, and $7 M_{\odot}$ (in each case using a boxcar method, as described above).

Within this grid, we look for the best-fitting model for each SN by minimizing χ^2 , which we calculate as

$$\chi^2 = \sum_{\lambda \in [g, \dots, z]} \sum_{t_S < t^* < t_{\text{PT}}} \frac{(M_{\lambda}^*(t^*) - M_{\lambda}(t^*))^2}{(\Delta M_{\lambda}^*(t^*))^2}, \quad (2)$$

where $M_{\lambda}^*(t^*)$ is the observed magnitude in a given band λ at the moment of observation t^* , $\Delta M_{\lambda}^*(t^*)$ is the corresponding observational error, and $M_{\lambda}(t^*)$ is the numerically obtained magnitude in the same band at the same moment of time. To take into account uncertainties in the explosion date, we shift the time of observations within the allowed range of explosion times in steps of 0.5 days, and look for the minimal χ^2 . In the first fitting step, we use only the parts of light curves between the time t_S and the end of plateau t_{PT} . We do not go beyond t_{PT} , since after this time, the whole ejecta is expected to become optically thin, and the diffusion approach to radiation transport used in SNEC is no longer valid. We do not include u -, U -, and B -bands in Equation (2) either, since after day ~ 20 the radiation in these bands is affected by iron-group line blanketing (Kasen & Woosley 2009), which is not taken into account. As a result of this first step, we obtain the best-fit values of progenitor ZAMS mass, explosion energy, degree of ^{56}Ni mixing, and explosion time.

For the second step, we attach CSM on top of these best-fitting RSG models, and we generate a grid of light curves in $R_{\text{ext}}-K$ parameter space for each SN. We vary K in the range between 1.0×10^{17} and 3.0×10^{18} in steps of 1.0×10^{17} , and R_{ext} in the range between 700 and $3800 R_{\odot}$ in steps of $100 R_{\odot}$. We shift the observational data with respect to the explosion date in the same way that minimized χ^2 during the first step. After this, we assess the best-fitting model within the $R_{\text{ext}}-K$ grid by calculating χ^2 as we did in Equation (2), but for $t^* < t_{\text{PT}}$ instead of $t_S < t^* < t_{\text{PT}}$. This second step results in the best-fitting values of the CSM density parameter K and external radius R_{ext} .

3.3. Numerical Results

Figures 2 and 3 show all of the best-fitting models for the SNe from our set, together with the observed light curves in different bands. The dashed lines show the result of the first fitting step (without CSM), while the solid lines show the final fit (with CSM). Residuals are shown to assess the quality of the fits. The shaded regions in the plots contain the data that were not used in our analysis for the reasons described in Section 3.2. For completeness, we partially show the radioactive tails of our light curves. We emphasize, however, that our code uses diffusion approach for the radiation transport, which works well for the shock cooling and plateau part of the light curve, but is not suitable for the nebular phase. In addition, as described in the code manual,⁶ for the purpose of magnitude calculations, the effective temperature is kept above 5000 K, following the reasoning of Swartz et al. (1991).

Therefore, no conclusion concerning the goodness of the fit can be made based on data after the end of plateau.

As emphasized in previous work (Morozova et al. 2017), we find that light curves obtained from the bare RSGs are significantly poorer at fitting the data than light curves that include dense CSM. The dashed curves in Figures 2 and 3 rise more slowly than the observations during the first 20–40 days (similar to Figures 2–4 of Morozova et al. 2017). On the other hand, if one were to restrict the fitting window for these models to just the time between the slope break and the end of plateau, then reasonable fits could be made with just bare RSGs. This lends support to the two-step method we used for the light-curve fitting. Interestingly, the addition of dense CSM even improves the fit of the early light curve in the B and U bands that we do not include when fitting. This is not surprising given that at the high effective temperatures of the early light curves (10,000 K and higher), the iron-group line blanketing does not play an important role and the spectrum is very close to a blackbody. Nevertheless, this is further evidence for the necessary presence of dense CSM.

Figures 4 and 5 illustrate the dependence of χ^2 on the grid parameters. Since the minimum of χ^2 in our models is rather shallow, it does not make much sense to access the confidence regions as we previously did in Morozova et al. (2017), because the 39.3% confidence region will cover $\sim 39.3\%$ of the domain, etc. Instead, we color-code the natural logarithm of $\chi^2/\chi_{\text{min}}^2$, so that the yellow contour in the figures approximately corresponds to the increase of χ^2 by a factor of e with respect to the minimum, while the green region corresponds to an order-of-magnitude increase. We adopt the extents of the yellow contours as the error estimates of our fits. Shaded gray regions in Figure 4 indicate the part of the domain that could not be covered by the light curves due to numerical difficulties, while in Figure 5 they just cut away the regions smaller than the radii of the underlying RSGs.

Figure 4 shows that the explosion energy is generally better constrained by our models than the progenitor ZAMS mass. The pre-explosion profiles of the progenitors are determined by complex nuclear burning processes during stellar evolution and do not always demonstrate smooth dependence on the ZAMS mass, which results in striped patterns in Figure 4. Figure 5 demonstrates a strong degeneracy between the density and the radial extent of the CSM. It is interesting to note, however, that the contours of constant χ^2 follow the contours of constant CSM mass very closely, which we plotted in the figure with white dashed lines. This tells us that the total mass of the CSM can be inferred from our fits more robustly than its density and external radius separately (as has been found for extended material in other types of SNe; Piro et al. 2017). As for the CSM radius, it is only a few times the RSG radius in all cases. This indicates that whatever causes the mass loss must occur at the very last stages of the RSG life.

All fitting parameters are summarized in Table 2. The different degrees of ^{56}Ni mixing result in rather close, and in some cases even identical, fitting progenitor characteristics (the best-fitting model of the three mixing degrees is shown in bold). The energy released in the radioactive decay of ^{56}Ni is expected to prolong the plateau and/or flatten it (Nakar et al. 2016). In our grid, however, this subtle effect is smeared by others, such as discontinuities in the properties of the progenitor models themselves, and the difference in fitting

⁶ https://stellarcollapse.org/codes/snecc_notes-1.00.pdf

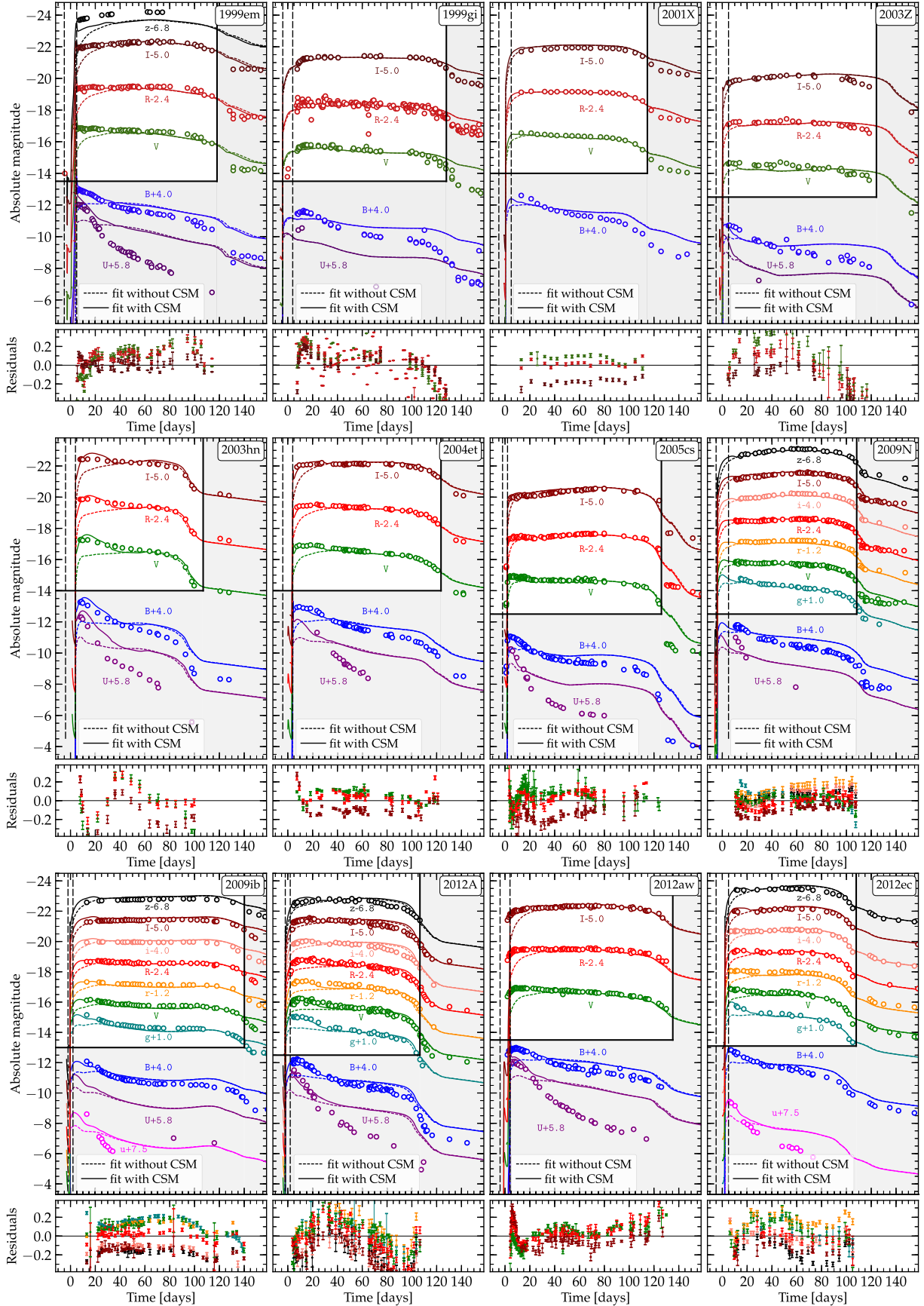


Figure 2. Best-fit light curves with (solid lines) and without (dashed lines) CSM. Data are shown as open circles. Each color corresponds to a different wave band as labeled. Unshaded (white) regions contain the SN data used to find the fits, while shaded (gray) regions are ignored for fitting either because it is too late in the light curve, or because iron-group line blanketing may be important (in the bluer bands).

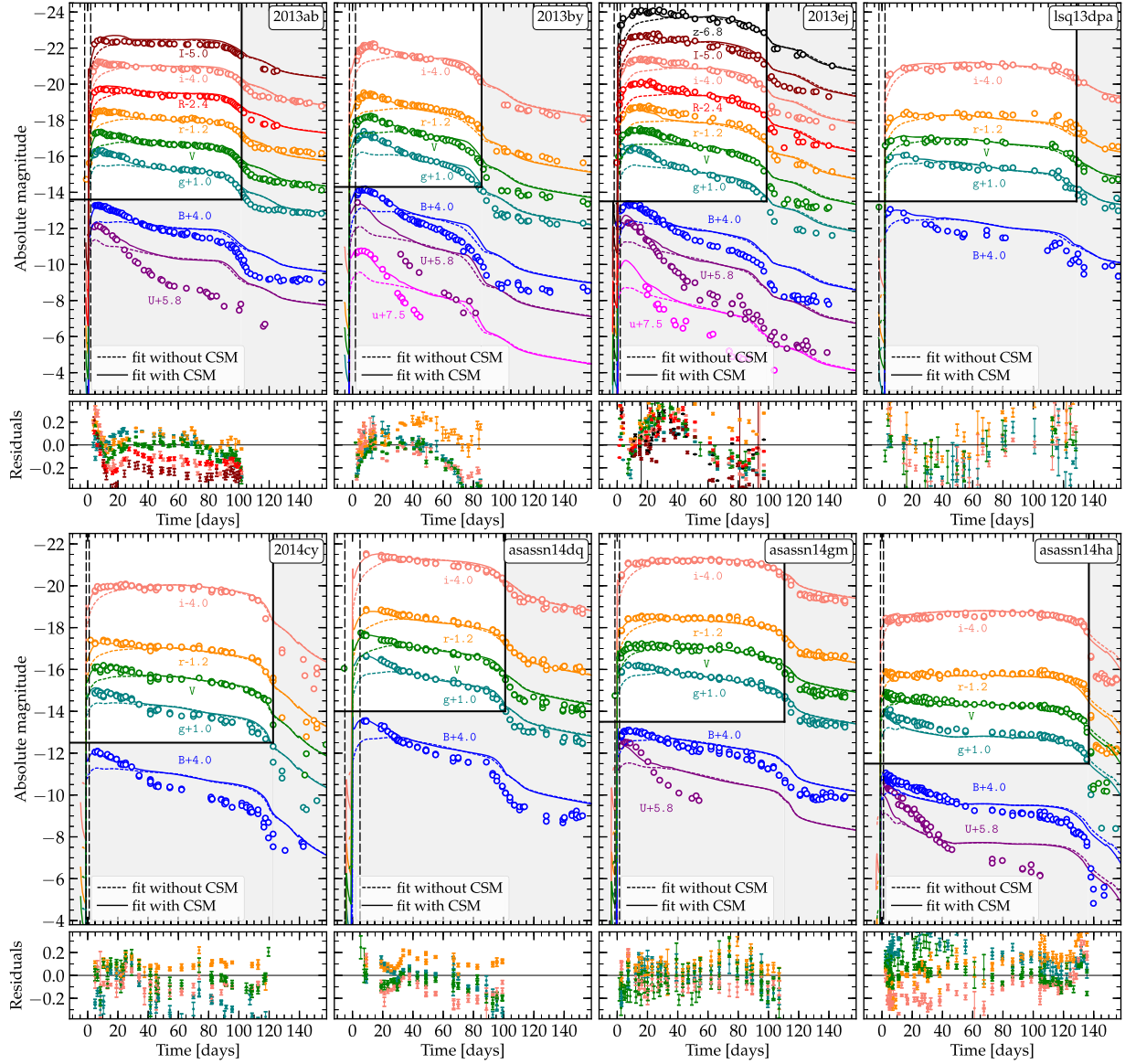


Figure 3. Additional SNe, the same as Figure 2.

parameters between the different mixing degrees is smaller than the error bars we estimate based on Figure 4.

As for the CSM, we added to the table its total mass M_{CSM} , without trying to convert it into the mass losses in $M_{\odot} \text{ yr}^{-1}$, which can be easily estimated from Equation (1) for a reasonable wind speed. In fact, there is no reason to assume a wind speed of 10 km s^{-1} , which is commonly observed in steady-state RSG winds. Higher wind velocities of $\sim 100 \text{ km s}^{-1}$ in our models would correspond to higher mass-loss rates on the order of few $M_{\odot} \text{ yr}^{-1}$ and the duration of the enhanced mass-loss period of only few months before explosion. However, since our models are not sensitive to the wind velocity in the pre-explosion models but rather to the density profile of the wind, we cannot place any constraint on the mass-loss rate and the duration of the outflow. Moreover, we emphasize that it is entirely possible that the dense CSM is not exactly a wind but a different density distribution for which the wind profile we use is an approximation. The origin of the CSM is an interesting topic of investigation on its own, and it lies beyond the scope of this study, although we discuss it further below.

It is worth noting that Morozova et al. (2017) also modeled two SNe from the current sample, 2013ej and 2013by, but using a

slightly different approach. They generated entire four-dimensional grids of light curves in M_{ZAMS} , E_{fin} , K , and R_{ext} parameter space, instead of using the two-step fitting procedure described here. This previous approach was more computationally expensive, which translated into a coarser resolution of these parameters. Morozova et al. (2017) obtained for SN 2013ej values of $M_{\text{ZAMS}} = 12.5 M_{\odot}$, $E_{\text{fin}} = 0.6 \text{ B}$, $K = 1.0 \times 10^{18} \text{ g cm}^{-1}$, and $R_{\text{ext}} = 2100 R_{\odot}$, and for SN 2013by, they obtained $M_{\text{ZAMS}} = 14.5 M_{\odot}$, $E_{\text{fin}} = 1.4 \text{ B}$, $K = 1.0 \times 10^{18} \text{ g cm}^{-1}$, and $R_{\text{ext}} = 2300 R_{\odot}$, both of which are in good agreement with the values from Table 2. This adds additional credence to the scheme we use in the current work. Unfortunately, we were unable to fit SN 2013fs using the two-step approach because of the lack of data near the transition between the plateau and radioactive tail.

4. Discussion

With the results from Section 3.3, we have for the first time ZAMS masses and dense CSM properties for a collection of Type II SNe based solely on light-curve fitting. This allows us to compare the parameters we measure with other studies in the

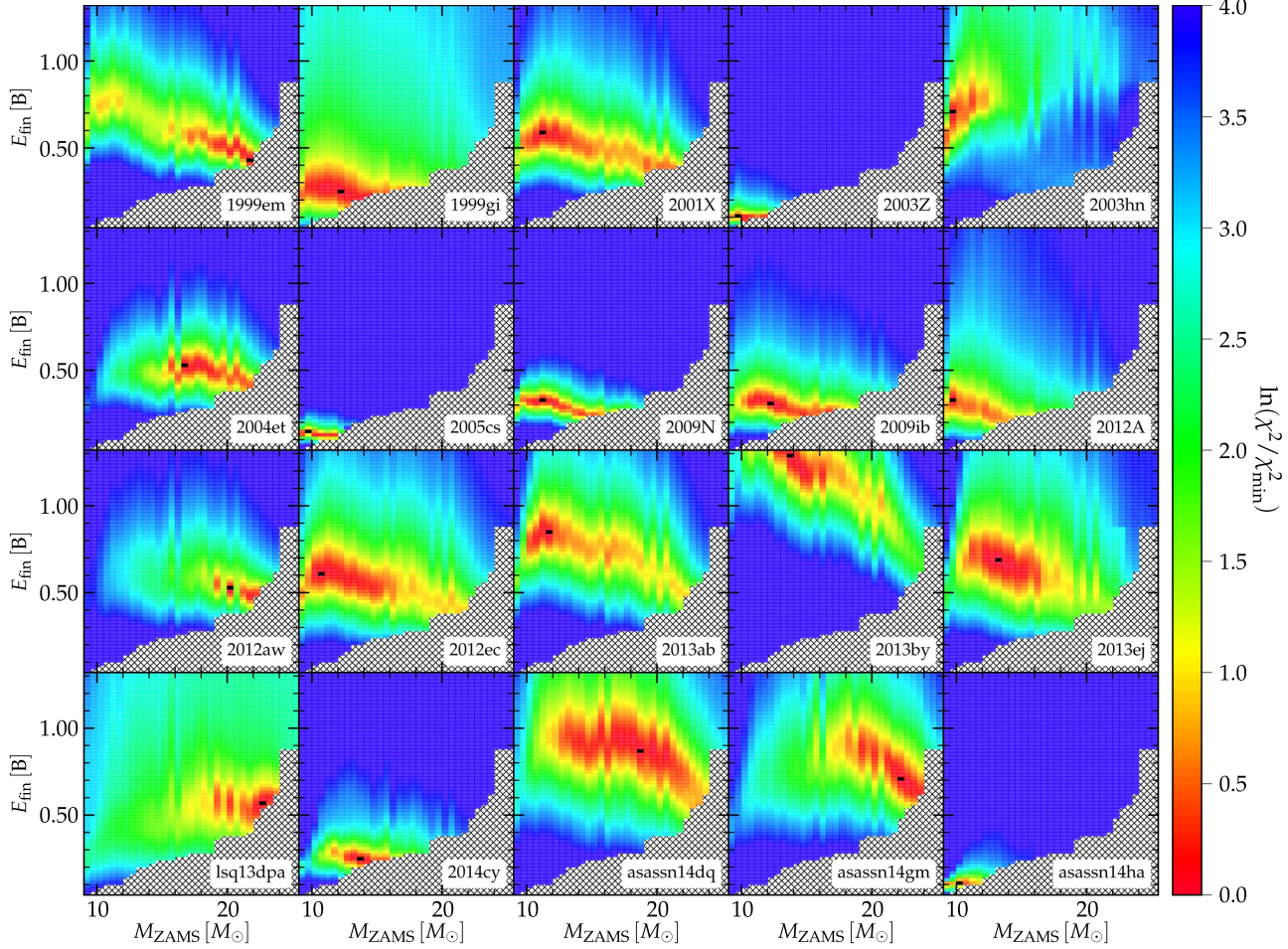


Figure 4. Color-coded ratio of χ^2 to χ^2_{\min} at each grid point in $M_{\text{ZAMS}} - E_{\text{fin}}$ space. The yellow contour approximately corresponds to the χ^2 increase by a factor of e with respect to the minimum. The black square in each panel indicates the best-fitting parameters. Gray shaded regions could not be covered by the current study due to the numerical difficulties. For each SN, the plotted χ^2 corresponds to the best-fitting degree of ^{56}Ni .

literature that used different methods to constrain the properties of SN II progenitors. Furthermore, we can look for correlations between the various parameters with the hope for a better understanding of the explosion mechanism as well as the origin of the dense CSM. We discuss each of these comparisons below.

4.1. Ejecta Masses

Figure 6 compares the ejecta masses and explosion energies obtained in our work to the other recently published studies of Utrobin & Chugai (2013) and Pumo et al. (2017); who, together with their own, collect the results of Tomasella et al. 2013, Dall’Ora et al. 2014, Spiro et al. 2014, Takáts et al. 2014, 2015, Bose et al. 2015, and Huang et al. 2015). This figure contains only the values obtained from the hydrodynamical models of the corresponding events, and does not include the numerous estimates obtained from the analytical scalings, spectra or X-ray/radio signals (see, among many others, Misra et al. 2007, Jerkstrand et al. 2012, 2014, Chakrabarti et al. 2016, Dhungana et al. 2016, and Yuan et al. 2016). These values are collected in the last column of Table 2. Some of the SNe that are common between samples are marked with special symbols.

For almost all of the SNe (with the exception of SN 2013ab), we obtain lower ejecta masses and energies than the previous

work. At least part of this difference arises because we used stellar evolution progenitor models instead of the double polytropic models that are widely used in the literature. The difference between evolutionary and non-evolutionary models that are capable of fitting the observational data equally well has been investigated by Utrobin et al. (2017) for SN 1999em. We add to this by comparing non-evolutionary and evolutionary models for SNe 2005cs and 2004et in Figure 7. For the evolutionary profiles, we show our best-fit models from Section 3, while the polytropic models are from Utrobin & Chugai (2008) and Utrobin & Chugai (2009). Figure 7 shows that the non-evolutionary models predict considerably higher progenitor masses than the evolutionary models. It is known from the analytical scalings (Arnett 1980; Chugai 1991; Popov 1993) that there is a certain degeneracy in the way the ejecta mass and the explosion energy influence the luminosity and duration of the light curve. Increasing the explosion energy makes the plateau shorter but more luminous, and so does decreasing the ejecta mass. This explains why more massive non-evolutionary progenitors also require higher explosion energies in order to reproduce the observed light curves. It is worth noting that the difference in the fitting models shown in Figure 7 is probably not due to the difference in the numerical codes, because with SNEC we were able to successfully reproduce the fit of SN 1999em from Bersten et al. (2011); very

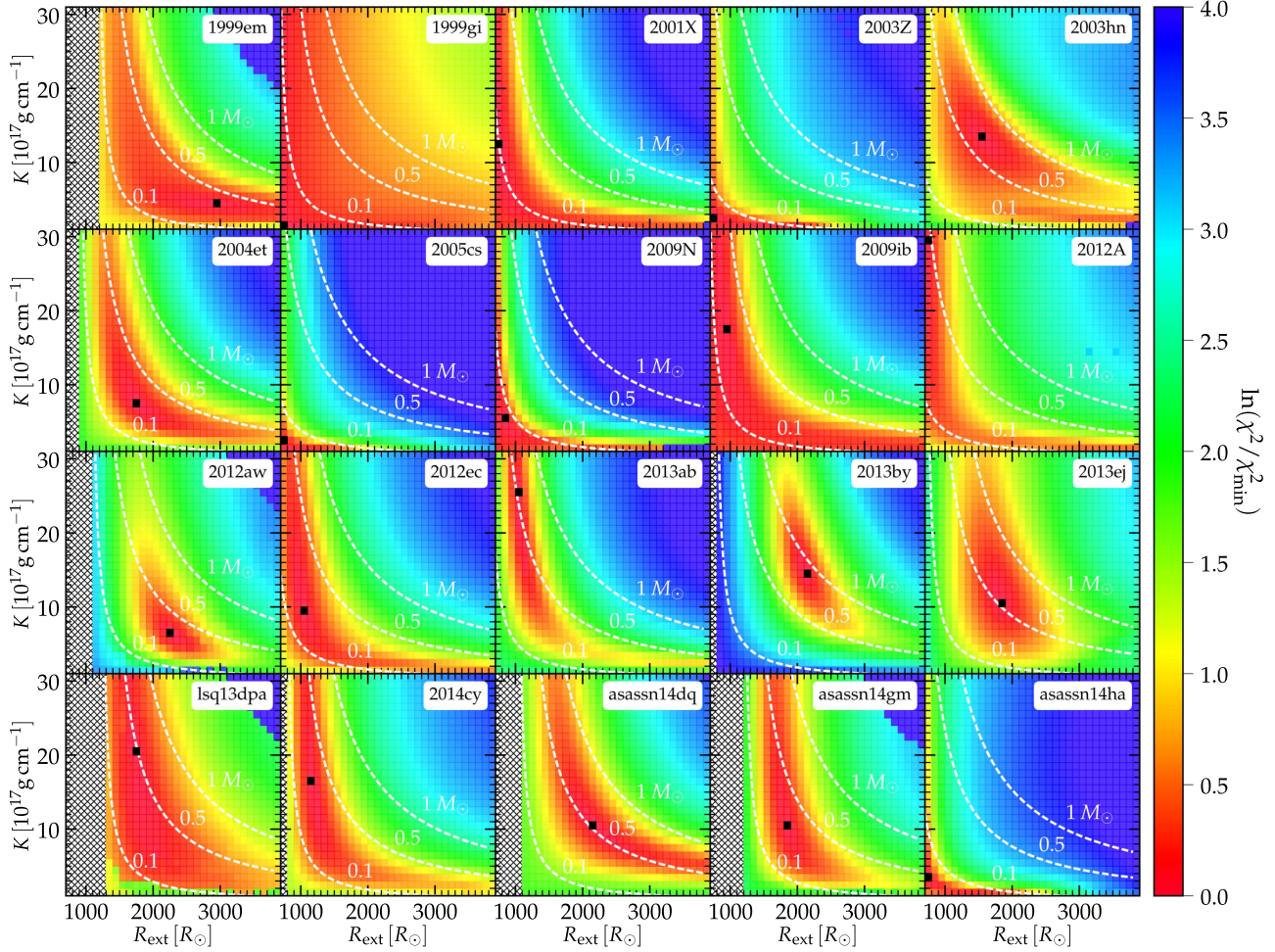


Figure 5. Color-coded ratio of χ^2 to χ^2_{\min} at each grid point in $R_{\text{ext}} - K$ space. The yellow contour approximately corresponds to the χ^2 increase by a factor of e with respect to the minimum. The black square in each panel indicates the best-fitting parameters. Shaded with gray are the regions below the RSG radius of the best-fitting model for the corresponding SNe. White lines show the constant CSM mass contours (0.1, 0.5, and $1 M_{\odot}$).

similar to the one from Utrobin (2007), using the same double polytropic model (see Appendix A of Morozova et al. 2015).

Our results from Figure 6 show less of a correlation between ejecta mass and explosion energy, but at the same time, all three samples show a lack of high ejecta masses with low energies. Although it is true that we did not consider some regions of this parameter space due to the numerical issues, Figure 4 shows that most of the best-fitting models are not near this boundary of the modeled region. The correlation between the progenitor mass and the explosion energy was studied previously, for example, in Poznanski (2013).

4.2. Progenitor ZAMS Masses

It is interesting to examine our results in view of the RSG problem, which has first been described in Smartt et al. (2009). The problem is that analysis of the archival pre-explosion images of SNe IIP implies an upper limit of $\sim 17 M_{\odot}$ for the ZAMS mass of their progenitors. This is significantly lower than the expected limit of $\sim 25 M_{\odot}$, obtained from the comparison of the observed properties of RSGs with their possible evolutionary tracks (Levesque et al. 2005, 2006). In addition, models of light curves of the same SNe are known to predict higher progenitor masses than those derived from the direct imaging (Utrobin & Chugai 2008, 2009).

The reason for this discrepancy may lie either on the observational side, on the theoretical side, or both. On the observational side, Walmswell & Eldridge (2012) proposed that extinction due to the circumstellar dust helps to increase the progenitor masses derived from the pre-explosion images. However, in subsequent work, Kochanek et al. (2012) demonstrated that the effects of dust composition, photon scattering, and near-IR dust emission may instead lead to an even lower progenitor mass estimate. On the theoretical side, the problem may come from the progenitor models or various physical approximations used in the codes. Finally, it is possible that stars with ZAMS masses in the range $17\text{--}25 M_{\odot}$ may evolve past the RSG stage due to enhanced mass loss or binary interactions and eventually explode as SNe of other types rather normal Type II (IIb/n or even Ib/c; see Smith et al. 2011).

The upper limit for the ZAMS mass of SNe II progenitors could signify that more massive stars collapse to black holes. They might eject their hydrogen envelope in a low-energy explosion (as described by Nadezhin 1980, Lovegrove & Woosley 2013, Piro 2013, and Lovegrove et al. 2017, and as potentially observed by Adams et al. 2017) rather than a typical SN. Such a process would then imply that the helium core masses of these stars become the black hole masses (Kochanek 2014; Clausen et al. 2015). Therefore the inferred

Table 2
Best-fit Parameters

SN	^{56}Ni Mixed to $3 M_{\odot}$		^{56}Ni Mixed to $5 M_{\odot}$		^{56}Ni Mixed to $7 M_{\odot}$		CSM Parameters			Best-fit M_{ej}	
	M_{ZAMS}	E_{fin}	M_{ZAMS}	E_{fin}	M_{ZAMS}	E_{fin}	K	R_{ext}	M_{CSM}	This Work	Other Works
1999em	21.5	0.42	20.5	0.52	20.0	0.48	4.0×10^{17}	2900	0.31	14.48	19 ^a
1999gi	12	0.24	12	0.22	10.5	0.22	1.0×10^{17}	700	<0.003	9.42	...
2001X	11	0.58	12	0.5	12.0	0.46	1.2×10^{18}	700	<0.07	9.29	...
2003Z	9.5	0.1	10	0.08	10	0.08	2.0×10^{17}	700	<0.03	7.81	14 ^a , 11.3 ^b
2003hn	9.5	0.76	9.5	0.7	9.5	0.66	1.3×10^{18}	1500	0.63	7.81	...
2004et	20	0.42	18	0.54	16.5	0.52	7.0×10^{17}	1700	0.25	12.47	22.9 ^a
2005cs	9.5	0.14	9.5	0.14	9.5	0.14	2.0×10^{17}	700	<0.03	7.81	15.9 ^a , 9.5 ^c
2009N	10	0.34	11	0.34	11	0.32	5.0×10^{17}	800	0.05	9.29	11.5 ^d
2009ib	12	0.3	14.5	0.24	12.5	0.24	1.7×10^{18}	900	0.2	9.42	15 ^e
2012A	9.5	0.32	9.5	0.3	9.5	0.3	2.9×10^{18}	700	<0.38	7.81	12.5 ^f
2012aw	20	0.52	20	0.52	20	0.52	6.0×10^{17}	2200	0.3	14.04	19.6 ^g
2012ec	10.5	0.68	10.5	0.64	10.5	0.6	9.0×10^{17}	1000	0.18	8.71	...
2013ab	11.5	0.84	12	0.76	11.5	0.7	2.5×10^{18}	1000	0.48	9.20	7 ^h
2013by	13.5	1.28	12.5	1.3	12.5	1.28	1.4×10^{18}	2100	0.83	10.16	-
2013ej	13	0.68	13.5	0.66	13	0.66	1.0×10^{18}	1800	0.49	9.95	10.6 ⁱ
LSQ13dpa	20	0.56	20	0.56	22.5	0.56	2.0×10^{18}	1700	0.43	14.30	...
2014cy	13.5	0.24	13.5	0.24	13.5	0.24	1.6×10^{18}	1100	0.25	10.16	...
ASASSN-14dq	19.5	0.86	18.5	0.86	18.5	0.86	1.0×10^{18}	2100	0.48	13.13	...
ASASSN-14gm	23.5	0.62	23.5	0.62	22	0.7	1.0×10^{18}	1800	0.27	14.40	...
ASASSN-14 ha	10	0.1	10	0.1	10	0.1	3.0×10^{17}	700	<0.03	8.25	...

Notes. Bold parameters highlight those with the smallest χ^2 of the three degrees of ^{56}Ni mixing. These values are shown in Figures 2–5 of Section 3 and used for the analysis of Section 4. All masses and radii are given in solar units, energies in B, and parameter K in g cm $^{-1}$. The last column lists the values used in Figure 6 only and is not meant to fully represent the numerous literature (see more references in the text).

^a Utrobin & Chugai (2013).

^b Pumo et al. (2017).

^c Spiro et al. (2014).

^d Takáts et al. (2014).

^e Takáts et al. (2015).

^f Tomasella et al. (2013).

^g Dall’Ora et al. (2014).

^h Bose et al. (2015).

ⁱ Huang et al. (2015).

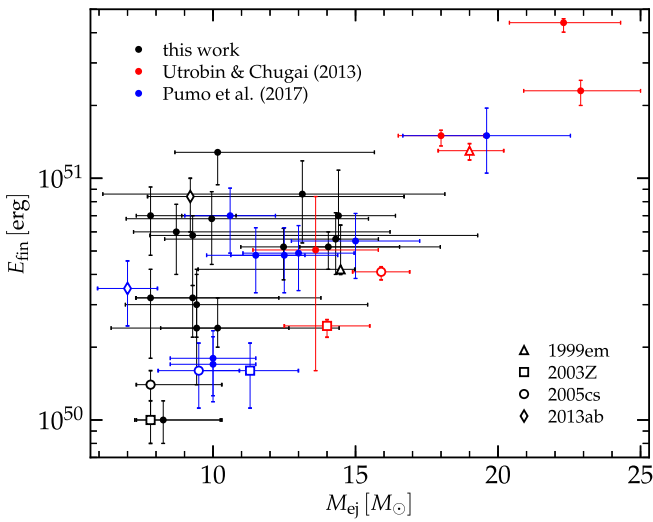


Figure 6. Ejecta masses vs. explosion energies derived for our sample of 20 SNe (black symbols), compared to the results of previous works. The error bars for our values are estimated based on the extent of the yellow contours in Figure 4, for Utrobin & Chugai (2013) based on their Figure 8, and for Pumo et al. (2017) taken to be 30% of the value of energy and 15% of the value of mass, as suggested by the authors.

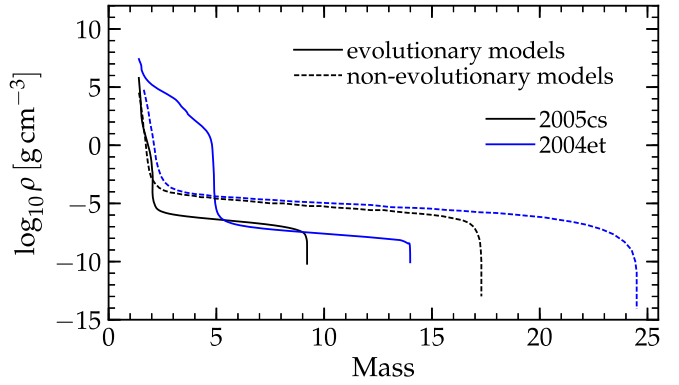


Figure 7. Comparison of the evolutionary and non-evolutionary models that produce numerical light curves (using different explosion energies) that compare favorably to the observations of SNe 2005cs and 2004et.

maximum mass for SN II progenitors may or may not explain the observed distribution of Galactic black hole masses (Özel et al. 2010) and the origin of a potential mass gap between neutron stars and black holes (Özel et al. 2012).

The top panel of Figure 8 shows eight SNe from our sample that also have an estimate of the progenitor ZAMS mass obtained from the pre-explosion imaging. All values shown

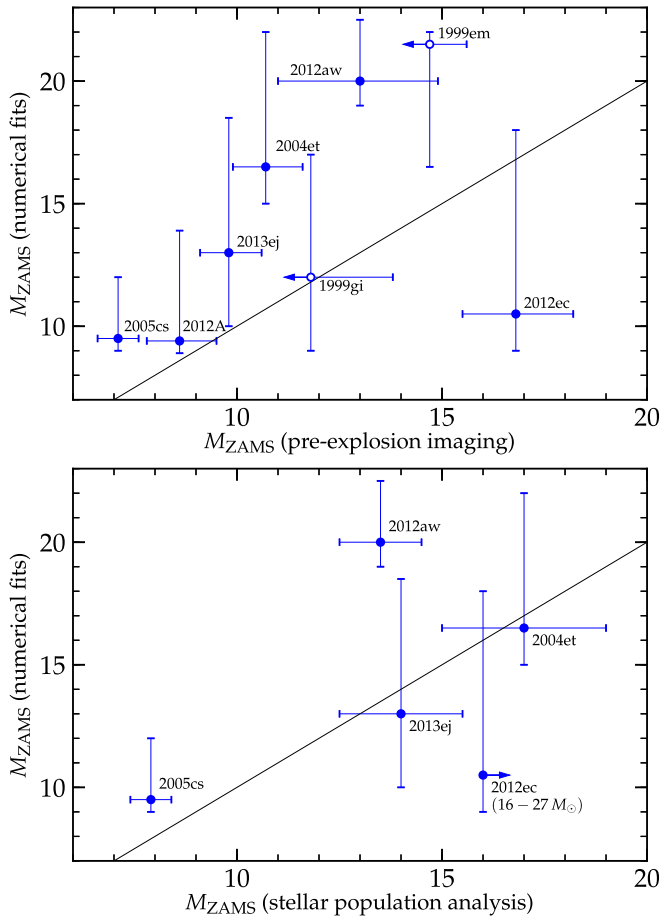


Figure 8. Top panel: Comparison of ZAMS masses of eight SNe obtained from our numerical fits with those obtained with the pre-explosion imaging (Davies & Beasor 2018; filled symbols indicate the progenitor detections, while empty symbols with arrows indicate upper limits from progenitor non-detections). The poor agreement between the ZAMS masses may at least be partly explained by the difference between the progenitor models from the evolutionary codes STARS and KEPLER (Jerkstrand et al. 2014; see the discussion in the text). Bottom panel: Comparison of ZAMS masses of SNe obtained from our numerical fits with those obtained from the analysis of the surrounding stellar populations by Maund (2017).

along the x -axis of Figure 8 are taken from the recent work of Davies & Beasor (2018), which summarizes and corrects the previous pre-explosion imaging mass estimates using updated bolometric corrections for RSGs. Earlier analyses of the pre-explosion images for the SNe shown in Figure 8 may be found in Walmswell & Eldridge (2012), Tomasella et al. (2013), Maund et al. (2013, 2014), Fraser et al. (2014), Fraser (2016), Kochanek et al. (2012), and Mauerhan et al. (2017). We use filled symbols for SNe with direct progenitor detections and the empty symbols for SNe that only have upper limits due to a non-detection of the progenitor.

At a first glance, the agreement between the masses obtained from the pre-explosion imaging and the hydrodynamical modeling in Figure 8 does not look good. However, it is important to note that these two parts of the analysis currently use progenitor models from different stellar evolution codes (STARS is used in Davies & Beasor 2018, and KEPLER in our work). The progenitor models from these two evolutionary codes are compared in Figure 5 of Jerkstrand et al. (2014), which demonstrates that for the same pre-explosion luminosity, the STARS models predict systematically lower ZAMS masses.

The difference between the STARS and KEPLER masses is about $1\text{--}2 M_{\odot}$ in the lower ZAMS mass range ($10\text{--}15 M_{\odot}$) and up to $4 M_{\odot}$ in the higher ZAMS mass range ($20\text{--}25 M_{\odot}$). Were the ZAMS masses in Figure 8 shifted correspondingly to the right along the x -axis, this would improve the agreement with the results of our modeling. We note that our M_{ZAMS} values for most of the SNe are lower than some of the other values previously obtained in the literature (Maguire et al. 2010; Dall’Ora et al. 2014).

The bottom panel of Figure 8 shows five SNe from our sample that have an estimate of the progenitor ZAMS mass obtained from the analysis of the surrounding stellar populations by Maund (2017). In this panel, SNe 2013ej and 2004et show better agreement with the numerical models than in the top panel. An interesting exception is SN 2012ec, for which the analysis of both pre-explosion images and stellar populations predicts a considerably higher ZAMS mass than the numerical modeling.

We next explore the ZAMS mass distribution implied by our sample. To do this, we consider a Salpeter initial mass function (IMF) and investigate the lower and upper limits on the progenitor ZAMS mass, M_{\min} and M_{\max} , respectively, that are needed to match our distribution. Following Smartt et al. (2009), we calculate the probability function for each SN in Table 2 as

$$P_j = \int_{M_{j,\text{low}}}^{M_j} \frac{(M - M_{j,\text{low}}) M_j^{\Gamma-1}}{(M_j - M_{j,\text{low}})(M_{\min}^{\Gamma} - M_{\max}^{\Gamma})} dM + \int_{M_j}^{M_{j,\text{high}}} \frac{M^{\Gamma-1}}{(M_{\min}^{\Gamma} - M_{\max}^{\Gamma})} dM, \quad (3)$$

where M_j is the best-fitting ZAMS mass of the j th SN, $M_{j,\text{low}}$ and $M_{j,\text{high}}$ are its lower and upper uncertainties, and $\Gamma = -1.35$ for the Salpeter IMF. When $M_{j,\text{low}}$ or $M_{j,\text{high}}$ are higher or lower than M_{\min} or M_{\max} , we use the latter as the integration limits. The maximum likelihood, calculated as $\mathcal{L} = \prod P_j$, corresponds to $M_{\min} = 10.4 M_{\odot}$ and $M_{\max} = 22.9 M_{\odot}$, as shown in black in the top panel of Figure 9. The 68%, 90%, and 95% confidence regions are estimated from the condition

$$\ln \mathcal{L}_{\max} - \ln \mathcal{L} = \frac{1}{2}\chi, \quad (4)$$

where $\chi = 2.3$, 4.6, and 6.2, correspondingly. The bottom panel of Figure 9 shows the cumulative frequency plot of the ZAMS masses derived from the numerical fit, analogous to the plot first published in Smartt et al. (2009) for the ZAMS masses derived from the pre-explosion images (their Figure 8). The solid line shows the Salpeter IMF with the minimum mass of $10.4 M_{\odot}$ and the maximum mass of $22.9 M_{\odot}$, derived from maximizing the likelihood.

For comparison with the pre-explosion imaging, in the top panel of Figure 9 we show the values for maximum and minimum masses obtained in Davies & Beasor (2018), using the stellar evolution codes STARS and KEPLER. This plot demonstrates that using the same set of progenitor models for the pre-explosion imaging and the hydrodynamical modeling improves the agreement between the mass limits. The maximum mass that we obtain is closer to the maximum mass of RSGs ($25\text{--}30 M_{\odot}$) seen from observations (Massey et al. 2001; Levesque et al. 2005, 2006; Crowther 2007). It therefore appears, returning to the discussion about RSGs above, that our distribution of masses mitigates some of the discrepancy in the RSG problem.

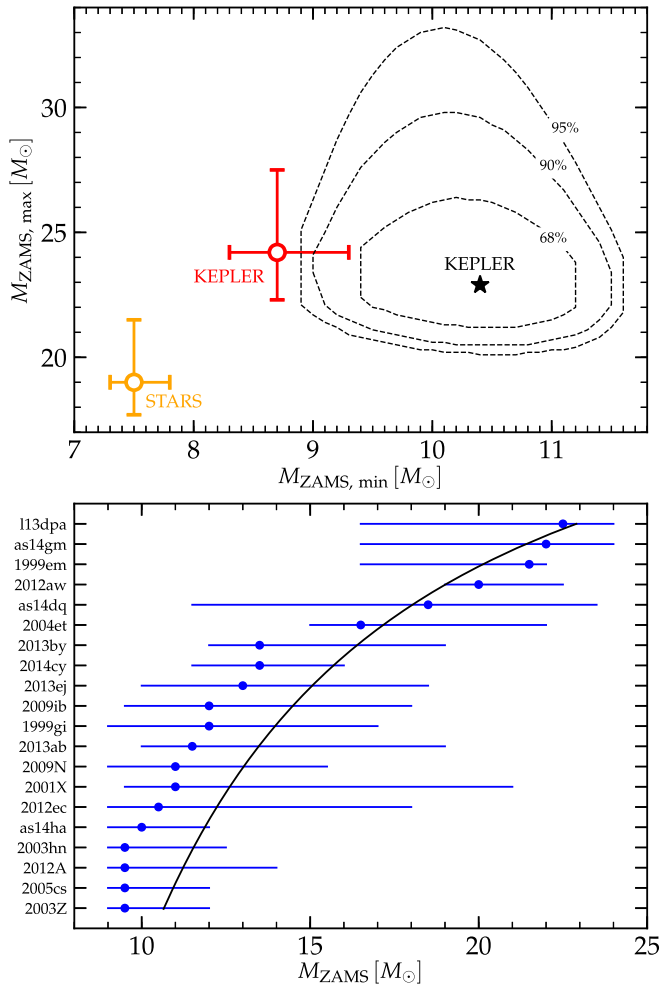


Figure 9. Top panel: Likelihood function for the minimum and maximum ZAMS masses of the Type II SN progenitors. The maximum likelihood derived from our numerical fits corresponds to $M_{\text{ZAMS, min}} = 10.4 M_{\odot}$ and $M_{\text{ZAMS, max}} = 22.9 M_{\odot}$, indicated by a black star in the plot. The contours show the 68%, 90%, and 95% confidence regions. For comparison, in yellow and red we show the values obtained in Davies & Beasor (2018) from the pre-explosion imaging, using the stellar evolution codes STARS and KEPLER, respectively. The estimates obtained with the same evolutionary code demonstrate better agreement, supporting our earlier discussion on Figure 8. Bottom panel: Cumulative frequency plot of the ZAMS masses derived from the numerical fits. The black line shows a Salpeter IMF with minimum and maximum ZAMS masses of 10.4 and $22.9 M_{\odot}$, respectively.

4.3. SN Explosion Properties

It is natural to assume that there must be a correlation between the explosion energy and the ^{56}Ni mass since this is synthesized as the shock propagates out through the dense regions of the core (Nadyozhin 2003). This correlation has previously been seen in nucleosynthetic simulations (Sukhbold et al. 2016) and light-curve parameterization methods (Pejcha & Thompson 2015). Furthermore, observations show these correlations through the ^{56}Ni mass and the plateau magnitudes of SNe II (Hamuy 2003; Spiro et al. 2014; Valenti et al. 2016) as well as their ejecta velocities (Maguire et al. 2012). Here we test whether this correlation is also seen simply from our light-curve fitting. Figure 10 compares the explosion energy derived from the numerical fits and the ^{56}Ni mass of the corresponding SNe. This shows a strong correlation between the two, similar to these other previous studies.

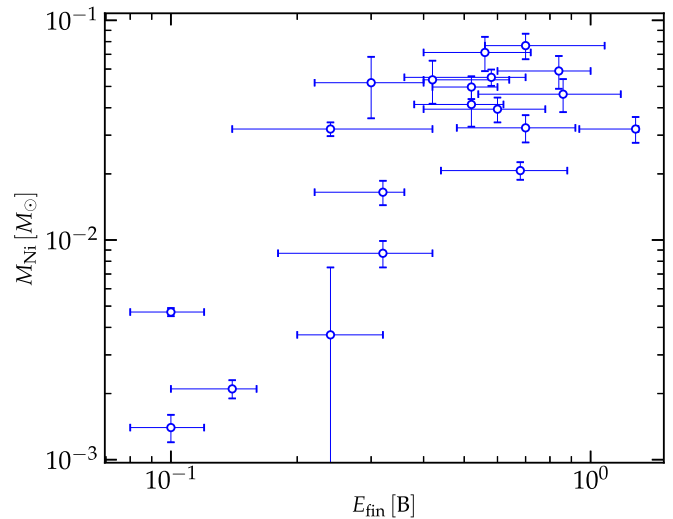


Figure 10. Correlation between the mass of ^{56}Ni and the explosion energy, obtained from our numerical fits.

4.4. CSM Properties

With our sample of SNe and models we can next address whether the CSM mass and radii we infer correlate with other properties of the SN or progenitor. This can hopefully provide clues about the mechanism that generates the dense CSM we find.

Figure 11 shows the derived CSM masses versus the ZAMS masses of the progenitors and the explosion energies. The arrows indicate events that only have an upper limit on the CSM mass. From the top panel, there does not appear to be a strong correlation between M_{CSM} and M_{ZAMS} . Nevertheless, all of the events where we only found CSM mass upper limits are below $M_{\text{ZAMS}} \sim 12 M_{\odot}$, which may be a result of our modeling or due to something physical that should be explored further.

On the other hand, the lower panel of Figure 11 suggests that there is indeed a correlation between M_{CSM} and the explosion energy. This general correlation was to be expected, since recent studies confirm that SNe IIL have somewhat higher explosion energies per unit ejecta mass than SNe IIP (see, e.g., Faran et al. 2014a; Gall et al. 2015) and the steeper decline of SNe IIL is due to a larger amount of dense CSM (Morozova et al. 2017). The important new finding here is that the correlation between M_{CSM} and explosion energy seems to extend continuously and roughly linearly throughout the entire sample. The meaning of this for the mechanism that generates the dense CSM is unclear. One possibility is that the process that generates the CSM also decreases the gravitational binding energy of the star. Then the mechanism that unbinds the star, commonly presumed to be neutrino heating, is more able to create a more energetic explosion.

Figure 12 shows the inferred radii of the CSM versus the ZAMS masses of the progenitors (top panel) and the explosion energies (bottom panel). There appears to be no clear correlation between R_{ext} and the explosion energy. On the other hand, there may be an indication that the dense CSM is more extended for larger M_{CSM} . This radius is related to both the duration and velocity of the CSM. Generally speaking, these values R_{ext} are only a few times higher than the progenitors' radii. This indicates that regardless of the velocity, the dense CSM must have been generated shortly before the explosion. For example, assuming the velocity of 10 km s^{-1} gives a timescale of mere years (and maybe just months for higher velocities). The advanced stages of nuclear burning

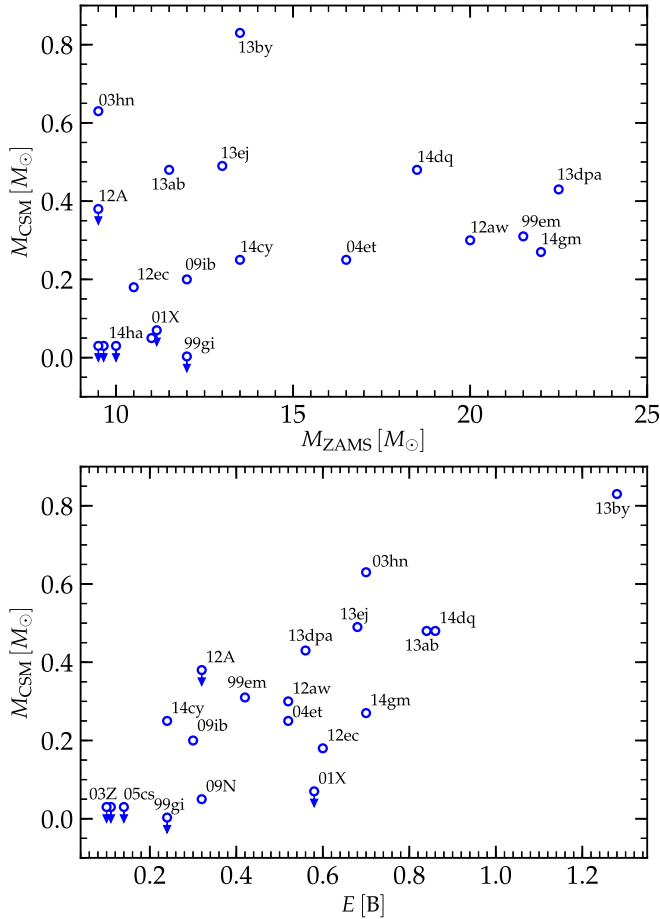


Figure 11. CSM mass vs. ZAMS mass (top panel) and explosion energy (bottom panel), obtained from our numerical light-curve fits. Arrows indicate SNe for which we only have upper limits on CSM mass from Table 2.

could act on such timescales, but the key issue is whether there is a way to harness the energy from this burning to generate the dense CSM. There have been a number of theoretical studies on how to generate pre-explosion outbursts: Yoon & Cantiello (2010), Arnett & Meakin (2011), Quataert & Shiode (2012), Shiode & Quataert (2014), Smith & Arnett (2014), Moriya & Langer (2015), Woosley & Heger (2015), and Quataert et al. (2016), and most recently, one of the most detailed studies of outbursts was modeled by Fuller (2017) using the open-source stellar evolution code MESA (Paxton et al. 2011, 2013, 2015). Nevertheless, it has yet to be shown that these mechanisms can reproduce exactly the dense CSM properties we need here.

4.5. Other Implications of Dense CSM

A number of observational works on the early SN II light curves point out that they typically rise faster than the analytical and hydrodynamical light curves obtained from standard RSG models (see, e.g., Gall et al. 2015; González-Gaitán et al. 2015). As a consequence, fitting the early SN II light curves with the analytical and numerical models resulted in relatively small ($\sim 500 R_{\odot}$) estimated radii of their progenitors (Dessart et al. 2013; González-Gaitán et al. 2015; Garnavich et al. 2016; see, however, Rubin et al. 2016; Shussman et al. 2016). These values are on the lower end of the radii estimated from the observations of galactic and Magellanic Cloud RSGs by Levesque et al. (2005) and

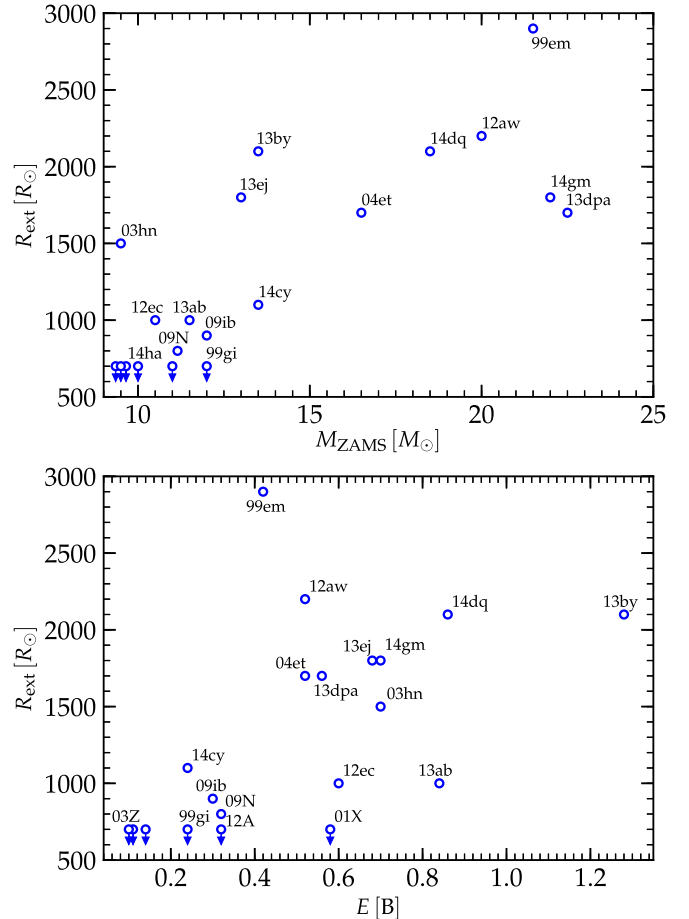


Figure 12. CSM radius vs. ZAMS mass (top panel) and explosion energy (bottom panel), obtained from the numerical light-curve fits. Arrows indicate SNe for which we only have upper limits on CSM mass from Table 2.

Levesque et al. (2006), which lie in the range between ~ 400 and $\sim 1500 R_{\odot}$. At the same time, a more recent study by Davies et al. (2013) suggests that the previous works could underestimate the RSG temperatures, and consequently, overestimate their radii. For comparison, the radii of the KEPLER models we use vary between ~ 400 and $\sim 1400 R_{\odot}$ without the CSM, and similar values for the models with the same ZAMS masses are obtained in Renzo et al. (2017). Our current study shows that adding dense CSM to otherwise standard RSGs leads to faster rise times, even though the total radius of the models increases. Figures 2 and 3 show that this effect is weaker for the ultraviolet bands, which can have the same rise time with and without CSM, but becomes very strong in red bands, where it is crucial for reproducing the early rise and maximum. Therefore, CSM may serve as an explanation of the fast rise of the early SN II light curves rather than the common explanation of changing the radius of the underlying RSGs.

Although we focus on photometric light curves, the presence of a dense CSM around otherwise normal SNe IIP has also been recently suggested by the spectroscopic observations of a number of events (see, e.g., Quimby et al. 2007; Kiewe et al. 2012; Yaron et al. 2017). The key is to obtain the spectra early enough, since the characteristic lines typically disappear within a day after the explosion. The material probed by these observations is lower in mass and larger in radius than what we study here (see discussions in Dessart et al. 2017; Yaron et al. 2017), so the exact relation between these two components of CSM is not clear. It is

important to note that in our models the shock breakout occurs at the very outer edge of the CSM. This means that at the moment when the first SN light is seen, the bulk of this CSM is optically thick and cannot contribute to the early spectrum. In addition, Dessart et al. (2017) have shown that a sharp transition between the low and high mass-loss states assumed in our models cannot reproduce the narrow emission lines observed, for example, in SN 2013fs. In reality, it is likely that there is a smoother transition between the dense CSM we model in this work and the regular low-density RSG wind. One interesting possibility to explain it is by employing an accelerating wind that evolves from being dense close to the star and less dense as it accelerates farther from the star (Moriya et al. 2017). In this case, the shock breaks out inside the wind, which changes the timescale of the breakout from the expected hours to days (Moriya et al. 2011). Such an extended shock breakout was seen, for example, in early observations of a Type II SN PS1-13arp by Gezari et al. (2015).

4.6. Limitations of SNEC

The numerical code we use applies some approximations and simplifications, so it is natural to ask how they affect our inferences of dense CSM. Generally speaking, a comparison between the light curves generated by SNEC and the multi-group radiation-hydrodynamic code STELLA (Blinnikov & Bartunov 1993, 2011; Baklanov et al. 2005; Blinnikov et al. 2006; Kozyreva et al. 2017) that uses the same RSG progenitor shows good agreement in the bolometric luminosity and plateau duration (P. Baklanov & S. Blinnikov 2018, private communication). Nevertheless, one of the largest discrepancies between the color light curves is seen during the early rise, where SNEC light curves rise consistently faster than STELLA light curves, reaching the same magnitudes $\sim 3 - 5$ days earlier.⁷ This can be explained by incomplete thermal equilibrium between the radiation and matter at the photosphere, which is captured by STELLA, but not by SNEC (the current version of SNEC uses the assumption of local thermodynamical equilibrium throughout the entire model). In the more realistic case, the observed temperature is set in a region deeper than the photosphere, where radiation processes are able to couple the gas and radiation (Nakar & Sari 2010). The value of the observed temperature is therefore higher, and it takes longer for it to drop down to the values corresponding to the blackbody maxima in the optical bands. This leads to the slower rise in these bands, as found by STELLA. As a consequence, we expect that it would be even more challenging for the multi-group radiation-hydrodynamic codes to reproduce the observed SN IIP light curves using stellar evolution RSG models without invoking some sort of CSM. Therefore, the mass of the CSM needed to fit the light curves with these codes will probably be even higher than our estimates. This is roughly consistent with our modeling of SN 2013fs, where the CSM mass is estimated to be $0.47 M_{\odot}$ (Morozova et al. 2017) and the work of Moriya et al. (2017), where it is estimated to be $0.5 M_{\odot}$.

Another limitation is related to the stiff inner boundary in SNEC, which causes numerical problems when we explode high ZAMS mass progenitors with low explosion energies. In Figure 4, the SNe that are most strongly affected by this issue are 1999em, lsq13dpa, 2014cy, and asassn14ha. In order to

check how this alters the inference of minimum and maximum ZAMS masses of Type II progenitors, we excluded these four SNe from the set and repeated the analysis shown in Figure 9. Without these SNe, the minimum mass $M_{\text{ZAMS}, \min}$ does not change, while the maximum mass $M_{\text{ZAMS}, \max}$ changes only slightly from 22.9 to $22.5 M_{\odot}$. Therefore, the main conclusions of our study do not depend on this problem.

5. Conclusions

Using modeling of the multiband light curves of 20 SNe II, we have for the first time constrained the progenitor ZAMS mass, explosion energy, and the mass and radial extent of dense CSM. For 25% of the SNe we infer ZAMS masses higher than $\sim 17 M_{\odot}$, the maximum limit suggested by the pre-explosion imaging. We show that the mass distribution we infer for our sample is consistent with a Salpeter distribution, and the minimum and maximum ZAMS masses for the SNe II progenitors are equal to 10.4 and $22.9 M_{\odot}$, respectively. This is in rough agreement with the observed masses of RSGs and suggests a solution to the RSG problem.

Our results imply that dense CSM is very common among SNe IIP, at least 70% of our fits benefit substantially from including it in the model. The largest amount of CSM (in mass) is expected from IIL-like events, while underluminous SNe from the low-mass progenitors have the smallest amount. The radii of the CSM that we deduce are quite small, in the range of $\sim 800 - 3000 R_{\odot}$, which argues that the mechanism that generates the CSM occurs mere years if not months before the explosion. Given these short timescales, the formation of CSM may be related to the advanced stages of nuclear burning in the stellar interior, which have recently been studied as a mechanism for generating mass outbursts (see Quataert & Shiode 2012; Shiode & Quataert 2014; Woosley & Heger 2015; Quataert et al. 2016; Fuller 2017).

With this sample we are able to explore whether the properties of the dense CSM are related to other aspects of the progenitor or explosion. The main correlations we find are that higher ZAMS masses have CSM at larger radii and higher energy explosions have higher mass CSM. In the former case, this may be related to the time when the dense CSM is generated. In the latter case, there is a suggestion that what generates the dense CSM may also cause the progenitor star to explode more easily. The history of trying to understand how core-collapse SNe explode by way of the neutrino mechanism is of course many decades long, with more failure than success. One possible solution is that the mechanism that generates the dense CSM may also change the structure of the star in a critical way that could facilitate unbinding the star. Such a hypothesis will hopefully be explored in future theoretical work using non-standard RSG structures (motivated by the need to generate dense CSM) in the most sophisticated calculations that investigate the neutrino mechanism.

We acknowledge helpful discussions with and feedback from A. Burrows, N. Smith, J. Stone, and D. Radice. We thank P. Baklanov, S. Blinnikov, C. Ott, E. Sorokina, and T. Moriya for comparison between SNEC and STELLA light curves. Computations were performed on the TIGER cluster at Princeton University. V.M. acknowledges funding support from the Lyman Spitzer Professorship at Princeton University and NSF Grant AST-1714267. A.L.P. acknowledges financial support for this research from a Scialog award made by the Research Corporation for Science Advancement.

⁷ The largest disagreement is seen in the *U*- and *B*-band light curves, which drop faster in STELLA simulations after day ~ 20 because the iron line opacity is treated properly. Since we are aware of this problem in our simulations, which is the main reason we do not fit the observed light curves in *U*- and *B*-bands, we omit the discussion of this effect in the text.

ORCID iDs

Anthony L. Piro <https://orcid.org/0000-0001-6806-0673>
 Stefano Valenti <https://orcid.org/0000-0001-8818-0795>

References

- Adams, S. M., Kochanek, C. S., Gerke, J. R., Stanek, K. Z., & Dai, X. 2017, *MNRAS*, **468**, 4968
- Anderson, J. P., González-Gaitán, S., Hamuy, M., et al. 2014, *ApJ*, **786**, 67
- Arcavi, I., Gal-Yam, A., Cenko, S. B., et al. 2012, *ApJL*, **756**, L30
- Arnett, W. D. 1980, *ApJ*, **237**, 541
- Arnett, W. D., & Meakin, C. 2011, *ApJ*, **733**, 78
- Baklanov, P. V., Blinnikov, S. I., & Pavlyuk, N. N. 2005, *AstL*, **31**, 429
- Barbon, R., Ciatti, F., & Rosino, L. 1979, *A&A*, **72**, 287
- Bersten, M. C., Benvenuto, O., & Hamuy, M. 2011, *ApJ*, **729**, 61
- Blinnikov, S. I., & Bartunov, O. S. 1993, *A&A*, **273**, 106
- Blinnikov, S. I., & Bartunov, O. S. 2011, STELLA: Multi-group Radiation Hydrodynamics Code, Astrophysics Source Code Library, Astrophysics Source Code Library, ascl:[1108.013](https://ascl.net/1108.013)
- Blinnikov, S. I., Röpke, F. K., Sorokina, E. I., et al. 2006, *A&A*, **453**, 229
- Bose, S., Valenti, S., Misra, K., et al. 2015, *MNRAS*, **450**, 2373
- Bruenn, S. W., Lentz, E. J., Hix, W. R., et al. 2016, *ApJ*, **818**, 123
- Burrows, A., Vartanyan, D., Dolence, J. C., Skinner, M. A., & Radice, D. 2018, *SSRv*, **214**, 33
- Cardelli, J. A., Clayton, G. C., & Mathis, J. S. 1989, *ApJ*, **345**, 245
- Chakraborti, S., Ray, A., Smith, R., et al. 2016, *ApJ*, **817**, 22
- Chevalier, R. A., & Irwin, C. M. 2011, *ApJL*, **729**, L6
- Chugai, N. N. 1991, *SvAL*, **17**, 210
- Chugai, N. N., Chevalier, R. A., & Utrobin, V. P. 2007, *ApJ*, **662**, 1136
- Clausen, D., Piro, A. L., & Ott, C. D. 2015, *ApJ*, **799**, 190
- Crowther, P. A. 2007, *ARA&A*, **45**, 177
- Dall’Ora, M., Botticella, M. T., Pumo, M. L., et al. 2014, *ApJ*, **787**, 139
- Davies, B., & Beasor, E. R. 2018, *MNRAS*, **474**, 2116
- Davies, B., Kudritzki, R.-P., Plez, B., et al. 2013, *ApJ*, **767**, 3
- Dessart, L., Hillier, D. J., & Audit, E. 2017, *A&A*, **605**, A83
- Dessart, L., Hillier, D. J., Waldman, R., & Livne, E. 2013, *MNRAS*, **433**, 1745
- Dhungana, G., Kehoe, R., Vinko, J., et al. 2016, *ApJ*, **822**, 6
- Dwarkadas, V. V. 2014, *MNRAS*, **440**, 1917
- Faran, T., Poznanski, D., Filippenko, A. V., et al. 2014a, *MNRAS*, **445**, 554
- Faran, T., Poznanski, D., Filippenko, A. V., et al. 2014b, *MNRAS*, **442**, 844
- Fraser, M. 2016, *MNRAS*, **456**, L16
- Fraser, M., Maund, J. R., Smartt, S. J., et al. 2014, *MNRAS*, **439**, L56
- Fuller, J. 2017, *MNRAS*, **470**, 1642
- Gall, E. E., Polshaw, J., Kotak, R., et al. 2015, *A&A*, **582**, A3
- Garnavich, P. M., Tucker, B. E., Rest, A., et al. 2016, *ApJ*, **820**, 23
- Gezari, S., Jones, D. O., Sanders, N. E., et al. 2015, *ApJ*, **804**, 28
- González-Gaitán, S., Tominaga, N., Molina, J., et al. 2015, *MNRAS*, **451**, 2212
- Groh, J. H., Meynet, G., Georgy, C., & Ekström, S. 2013, *A&A*, **558**, A131
- Hamuy, M. 2003, *ApJ*, **582**, 905
- Huang, F., Wang, X., Zhang, J., et al. 2015, *ApJ*, **807**, 59
- Jerkstrand, A., Fransson, C., Maguire, K., et al. 2012, *A&A*, **546**, A28
- Jerkstrand, A., Smartt, S. J., Fraser, M., et al. 2014, *MNRAS*, **439**, 3694
- Kasen, D., & Woosley, S. E. 2009, *ApJ*, **703**, 2205
- Kiewe, M., Gal-Yam, A., Arcavi, I., et al. 2012, *ApJ*, **744**, 10
- Kochanek, C. S. 2014, *ApJ*, **785**, 28
- Kochanek, C. S., Khan, R., & Dai, X. 2012, *ApJ*, **759**, 20
- Kozyreva, A., Gilmer, M., Hirschi, R., et al. 2017, *MNRAS*, **464**, 2854
- Levesque, E. M., Massey, P., Olsen, K. A. G., et al. 2005, *ApJ*, **628**, 973
- Levesque, E. M., Massey, P., Olsen, K. A. G., et al. 2006, *ApJ*, **645**, 1102
- Li, W., Van Dyk, S. D., Filippenko, A. V., et al. 2006, *ApJ*, **641**, 1060
- Lovegrove, E., & Woosley, S. E. 2013, *ApJ*, **769**, 109
- Lovegrove, E., Woosley, S. E., & Zhang, W. 2017, *ApJ*, **845**, 103L
- Maguire, K., Di Carlo, E., Smartt, S. J., et al. 2010, *MNRAS*, **404**, 981
- Maguire, K., Jerkstrand, A., Smartt, S. J., et al. 2012, *MNRAS*, **420**, 3451
- Massey, P., DeGioia-Eastwood, K., & Waterhouse, E. 2001, *AJ*, **121**, 1050
- Mauerhan, J. C., Van Dyk, S. D., Johansson, J., et al. 2017, *ApJ*, **834**, 118
- Maund, J. R. 2017, *MNRAS*, **469**, 2202
- Maund, J. R., Fraser, M., Smartt, S. J., et al. 2013, *MNRAS*, **431**, L102
- Maund, J. R., Reilly, E., & Mattila, S. 2014, *MNRAS*, **438**, 938
- Misra, K., Pooley, D., Chandra, P., et al. 2007, *MNRAS*, **381**, 280
- Moriya, T., Tominaga, N., Blinnikov, S. I., Baklanov, P. V., & Sorokina, E. I. 2011, *MNRAS*, **415**, 199
- Moriya, T. J., & Langer, N. 2015, *A&A*, **573**, A18
- Moriya, T. J., Yoon, S.-C., Gräfener, G., & Blinnikov, S. I. 2017, *MNRAS*, **469**, L108
- Morozova, V., Piro, A. L., Renzo, M., et al. 2015, *ApJ*, **814**, 63
- Morozova, V., Piro, A. L., Renzo, M., & Ott, C. D. 2016, *ApJ*, **829**, 109
- Morozova, V., Piro, A. L., & Valenti, S. 2017, *ApJ*, **838**, 28
- Müller, B., Janka, H.-T., & Marek, A. 2012, *ApJ*, **756**, 84
- Nadezhin, D. K. 1980, *Ap&SS*, **69**, 115
- Nadyozhin, D. K. 2003, *MNRAS*, **346**, 97
- Nagy, A. P., & Vinkó, J. 2016, *A&A*, **589**, A53
- Nakar, E., Poznanski, D., & Katz, B. 2016, *ApJ*, **823**, 127
- Nakar, E., & Sari, R. 2010, *ApJ*, **725**, 904
- Ofek, E. O. 2014, MATLAB Package for Astronomy and Astrophysics, Astrophysics Source Code Library, Astrophysics Source Code Library, ascl:[1407.005](https://ascl.net/1407.005)
- Ofek, E. O., Rabinak, I., Neill, J. D., et al. 2010, *ApJ*, **724**, 1396
- Özel, F., Psaltis, D., Narayan, R., & McClintock, J. E. 2010, *ApJ*, **725**, 1918
- Özel, F., Psaltis, D., Narayan, R., & Santos Villarreal, A. 2012, *ApJ*, **757**, 55
- Paczyński, B. 1983, *ApJ*, **267**, 315
- Paxton, B., Bildsten, L., Dotter, A., et al. 2011, *ApJS*, **192**, 3
- Paxton, B., Cantiello, M., Arras, P., et al. 2013, *ApJS*, **208**, 4
- Paxton, B., Marchant, P., Schwab, J., et al. 2015, *ApJS*, **220**, 15
- Pejcha, O., & Thompson, T. A. 2015, *ApJ*, **801**, 90
- Piro, A. L. 2013, *ApJL*, **768**, L14
- Piro, A. L., Muhleisen, M., Arcavi, I., et al. 2017, *ApJ*, **846**, 94
- Popov, D. V. 1993, *ApJ*, **414**, 712
- Poznanski, D. 2013, *MNRAS*, **436**, 3224
- Pumo, M. L., Zampieri, L., Spiro, S., et al. 2017, *MNRAS*, **464**, 3013
- Quataert, E., Fernández, R., Kasen, D., Klion, H., & Paxton, B. 2016, *MNRAS*, **458**, 1214
- Quataert, E., & Shioide, J. 2012, *MNRAS*, **423**, L92
- Quimby, R. M., Wheeler, J. C., Höflich, P., et al. 2007, *ApJ*, **666**, 1093
- Radice, D., Burrows, A., Vartanyan, D., Skinner, M. A., & Dolence, J. C. 2017, *ApJ*, **850**, 43
- Renzo, M., Ott, C. D., Shore, S. N., & de Mink, S. E. 2017, *A&A*, **603**, 118
- Rubin, A., & Gal-Yam, A. 2017, *ApJ*, **848**, 8
- Rubin, A., Gal-Yam, A., De Cia, A., et al. 2016, *ApJ*, **820**, 33
- Sanders, N. E., Soderberg, A. M., Gezari, S., et al. 2015, *ApJ*, **799**, 208
- Shiode, J. H., & Quataert, E. 2014, *ApJ*, **780**, 96
- Shussman, T., Waldman, R., & Nakar, E. 2016, arXiv:[1610.05323](https://arxiv.org/abs/1610.05323)
- Smartt, S. J. 2009, *ARA&A*, **47**, 63
- Smartt, S. J., Eldridge, J. J., Crockett, R. M., & Maund, J. R. 2009, *MNRAS*, **395**, 1409
- Smith, N., & Arnett, W. D. 2014, *ApJ*, **785**, 82
- Smith, N., Li, W., Filippenko, A. V., & Chornock, R. 2011, *MNRAS*, **412**, 1522
- Spiro, S., Pastorello, A., Pumo, M. L., et al. 2014, *MNRAS*, **439**, 2873
- Sukhbold, T., Ertl, T., Woosley, S. E., Brown, J. M., & Janka, H.-T. 2016, *ApJ*, **821**, 38
- Sukhbold, T., & Woosley, S. E. 2014, *ApJ*, **783**, 10
- Summa, A., Hanke, F., Janka, H.-T., et al. 2016, *ApJ*, **825**, 6
- Suwa, Y., Yamada, S., Takiwaki, T., & Kotake, K. 2016, *ApJ*, **816**, 43
- Swartz, D. A., Wheeler, J. C., & Harkness, R. P. 1991, *ApJ*, **374**, 266
- Takáts, K., Pignata, G., Pumo, M. L., et al. 2015, *MNRAS*, **450**, 3137
- Takáts, K., Pumo, M. L., Elias-Rosa, N., et al. 2014, *MNRAS*, **438**, 368
- Tomasella, L., Cappellaro, E., Fraser, M., et al. 2013, *MNRAS*, **434**, 1636
- Utrobin, V. P. 2007, *A&A*, **461**, 233
- Utrobin, V. P., & Chugai, N. N. 2008, *A&A*, **491**, 507
- Utrobin, V. P., & Chugai, N. N. 2009, *A&A*, **506**, 829
- Utrobin, V. P., & Chugai, N. N. 2013, *A&A*, **555**, A145
- Utrobin, V. P., Wongwathanarat, A., Janka, H.-T., & Mueller, E. 2017, *ApJ*, **846**, 37
- Valenti, S., Howell, D. A., Stritzinger, M. D., et al. 2016, *MNRAS*, **459**, 3939
- Valenti, S., Sand, D., Stritzinger, M., et al. 2015, *MNRAS*, **448**, 2608
- Van Dyk, S. D., Cenko, S. B., Poznanski, D., et al. 2012, *ApJ*, **756**, 131
- Walmswell, J. J., & Eldridge, J. J. 2012, *MNRAS*, **419**, 2054
- Weaver, T. A., Zimmerman, G. B., & Woosley, S. E. 1978, *ApJ*, **225**, 1021
- Woosley, S. E., & Heger, A. 2007, *PhR*, **442**, 269
- Woosley, S. E., & Heger, A. 2015, *ApJ*, **810**, 34
- Yaron, O., Perley, D. A., Gal-Yam, A., et al. 2017, *NatPh*, **13**, 510
- Yoon, S.-C., & Cantiello, M. 2010, *ApJL*, **717**, L62
- Yuan, F., Jerkstrand, A., Valenti, S., et al. 2016, *MNRAS*, **461**, 2003
- Zaghoul, M. R., Bourham, M. A., & Doster, J. M. 2000, *JPhD*, **33**, 977